Supplementary materials for
High-resolution strain rate mapping around inland plate boundary within the volcanic arc
using L-band InSAR and dense GNSS networks

Shogo Nagaoka*, Youichiro Takada, Takuya Nishimura, Takeshi Sagiya, and Yusaku Ohta

*nagaoka-tsu1999@eis.hokudai.ac.jp

This document consists of four text sections, two supporting tables and thirteen supporting figures:

S1 InSAR time series analysis and uncertainty estimation

We estimated the InSAR line-of-sight (LOS) velocities and their uncertainties using a weighted least-squares inversion[1,2]. We defined the model vector $\mathbf{m}$ as the cumulative LOS displacement and related it to the data vector $\mathbf{d}$ as follows:

$$\mathbf{d} = \mathbf{Gm},$$

$$G_{i,j} = \begin{cases} -1 & (H_{i,1} = L_j), \\ 1 & (H_{i,2} = L_j), \\ 0 & \text{otherwise}, \end{cases} \tag{S1}$$

where $\mathbf{d} = \{d_i \mid i = 1, 2, \cdots, N\}$ is the LOS change of the i-th interferogram and $\mathbf{m} = \{m_j \mid j = 1, 2, \cdots, M-1\}$ is the cumulative LOS displacement relative to the first SAR acquisition; N is the number of interferograms and M is the number of SAR acquisitions. $H_{i,1}$ and $H_{i,2}$ denote the primary and secondary acquisition dates of the i-th interferogram, and L_j denotes the end-date of the cumulative displacement m_j, corresponding to the SAR acquisition that terminates the cumulative interval.

We quantified uncertainties of the interferograms using a theoretical standard deviation based on coherence[3,4]:

$$\sigma_\phi = \frac{1}{\sqrt{2N_L}} \frac{\sqrt{1-\gamma^2}}{\gamma}, \tag{S2}$$

where N_L is the effective number of looks (number of independent samples per pixel) and γ is the interferometric coherence. The square of σ_ϕ was assigned to the diagonal elements of the weighting matrix $\mathbf{W}$:

$$[\mathbf{W}]_{i,j} = [\mathrm{Cov}(\mathbf{d})]_{i,j} = \delta_{i,j} \sigma_\phi^2. \tag{S3}$$

The model vector was estimated as follows[5]:

$$\mathbf{m}^{\mathrm{est}} = [\mathbf{G}^{\mathrm{T}}\mathbf{W}\mathbf{G}]^{-1}\mathbf{G}^{\mathrm{T}}\mathbf{W}\mathbf{d}. \tag{S4}$$

The matrix $\mathbf{A}$ was defined as

$$\mathbf{A} = [\mathbf{G}^{\mathrm{T}}\mathbf{W}\mathbf{G}]^{-1}\mathbf{G}^{\mathrm{T}}\mathbf{W}. \tag{S5}$$

Then the covariance matrix of the model vector was obtained as

$$[\mathrm{Cov}(\mathbf{m})] = \mathbf{A}[\mathrm{Cov}(\mathbf{d})]\mathbf{A}^{\mathrm{T}}, \tag{S6}$$

The standard deviations of the cumulative displacements were obtained as the square root of the diagonal elements of $\mathrm{Cov}(\mathbf{m})$. We estimated the LOS velocity by fitting a line to the cumulative displacements (Supplementary Figure S2). We propagated the uncertainties $\mathrm{Cov}(\mathbf{m})$ to the subsequent strain rate calculations (Supplementary Figure S11) in the same way as describe above.

S2 InSAR long-wavelength noise correction

We used GNSS data to correct long-wavelength noise in the InSAR velocity fields[6,7]. First, the GNSS velocities (Figure 2) were projected onto the line-of-sight (LOS) directions of the InSAR measurements. Assuming that the GNSS velocities represent the true ground motion, we treated the difference between the two datasets as the residual noise in the InSAR velocities:

$$z_i^{\mathrm{res}} = z_i^{\mathrm{InSAR}} - z_i^{\mathrm{GNSS}}, \tag{S7}$$

where $z_i^{\mathrm{InSAR}}, z_i^{\mathrm{GNSS}}$ denote the LOS velocities estimated from InSAR and GNSS at the i-th station, respectively, and z_i^{res} is the residual. The residual was modeled as a planar surface:

$$z_i^{\mathrm{res}} = s + px_i + qy_i \tag{S8}$$

where x_i and y_i are the horizontal coordinates of the i-th station. The parameters p, q and s were estimated using a least-squares approach. We then constructed a planar surface that had the same size as the interferogram and subtracted it from all pixels to obtain the corrected InSAR velocities.

S3 GNSS data interpolation

To compute spatial gradients from the discrete GNSS velocity observations, we interpolated the GNSS velocities onto a regular grid using the Kriging method[8–10]. We first removed a long-wavelength polynomial surface (drift) from the GNSS north-south velocities (Figure 2b), using a least-squares method. After the trend removal, an experimental variogram $\gamma_E(h)$ was estimated from these velocities:

$$\gamma_E(h) = \frac{1}{2N(h)} \sum_{i=1}^{N(h)} (z_{x_i} - z_{x_i+h})^2, \tag{S9}$$

where z_{x_i} and z_{x_i+h} are the velocities separated by a distance of h, and $N(h)$ is the number of samples in the distance bins. We set the bin interval as 1 km and calculated the average values for every bin. Next, we fit the experimental variogram with a spherical model:

$$\gamma(h) = \begin{cases} b + (c-b)\left(1 - \frac{3}{2}\frac{h}{a} + \frac{1}{2}\frac{h^3}{a^3}\right), & (0 \leq h \leq a) \\ c, & (h > a) \end{cases} \tag{S10}$$

where a, b, and c are the range, nugget, and sill of the variogram, respectively. We performed the regression and obtained these constants of 8×10^4 m, 1.2×10^{-6} m^2 yr^{-2}, 3.3×10^{-6} m^2 yr^{-2}, respectively.

Using this variogram model, we interpolated the data into the regular grid by the weighted sum of the surrounding velocity data z_k. The weights λ_k, which minimize the expected variance, were determined by solving the following equation:

$$\sum_k \lambda_k C_{j,k} = C_{j,0}, \tag{S11}$$

where $C_{j,k}$, $C_{j,0}$ denote the covariance between the j-th and k-th, and j-th and target point x_0, respectively. The covariance matrix $C_{j,k}$ was constructed from both the variogram model $\gamma(h)$ and the standard deviation σ_k of k-th GNSS velocity[11, 12] as follows:

$$C_{j,k} = c - \gamma(h_{j,k}) + \delta_{j,k}\,\sigma_j\sigma_k, \tag{S12}$$

where $h_{j,k}$ is a distance between the j-th and k-th points, and $\delta_{j,k}$ is the Kronecker delta. By solving Equations S11 and S12 for the weights λ_k, we obtained the interpolated velocity z^* and its estimation variance $\mathrm{Var}(z^*)$ at the target point x_0:

$$z^* = \sum_k \lambda_k(z_k - m_0) + m_0,$$
$$\mathrm{Var}(z^*) = c - \sum_k \lambda_k C_{k,0}. \tag{S13}$$

Here, m_0 denotes the average velocity (drift) at x_0, previously estimated as a polynomial surface.

S4 Strain rate estimation

In order to calculate the strain rate tensor in a numerically robust way, we used a multi-point method. First, the eastward and northward velocities u, v within a circular area of radius R were extracted together with their horizontal coordinates x, y. We then fit a planar surface to these data to estimate the velocity gradients (Equation 2) using the weighted least-squares method[5]. In this procedure, the uncertainties of the east-west InSAR velocities (Supplementary Text S1) and the north-south GNSS velocities interpolated by the Kriging method (Supplementary Text S3) were incorporated into the weighting matrix. Then we obtained the velocity gradient tensor (Supplementary Figure S4) and the strain rate tensor:

$$\begin{bmatrix} e_{xx} & e_{xy} \\ e_{xy} & e_{yy} \end{bmatrix} = \begin{bmatrix} \frac{\partial u}{\partial x} & \frac{1}{2}\left(\frac{\partial v}{\partial x} + \frac{\partial u}{\partial y}\right) \\ \frac{1}{2}\left(\frac{\partial v}{\partial x} + \frac{\partial u}{\partial y}\right) & \frac{\partial v}{\partial y} \end{bmatrix}. \tag{S14}$$

Finally, we calculated the strain rate invariants:

$$I_1 = e_{xx} + e_{yy} = e_1 + e_2,$$
$$I_{max\_shear} = \sqrt{e_{xy}^2 + \frac{1}{4}(e_{xx} - e_{yy})^2} = \frac{1}{2}(e_1 - e_2),$$
$$I_2 = \sqrt{e_{xx}^2 + e_{yy}^2 + 2e_{xy}^2} = \sqrt{e_1^2 + e_2^2}, \tag{S15}$$

where e_1, e_2 are the maximum and minimum principal strain rates, and I_1, I_{max_shear} and I_2 are dilatation rate, maximum shear strain rate, and second invariant of the strain rate tensor, respectively.

References

1. Berardino, P., Fornaro, G., Lanari, R. & Sansosti, E. A new algorithm for surface deformation monitoring based on small baseline differential SAR interferograms. *IEEE Transactions on Geosci. Remote. Sens.* **40**, 2375–2383, DOI: 10.1109/TGRS.2002.803792 (2002).

2. Schmidt, D. A. & Bürgmann, R. Time-dependent land uplift and subsidence in the Santa Clara valley, California, from a large interferometric synthetic aperture radar data set. *J. Geophys. Res. Solid Earth* **108**, DOI: 10.1029/2002jb002267 (2003).

3. Rodriguez, E. & Martin, J. M. Theory and design of interferometric synthetic aperture radars. In *IEE Proceedings F (Radar and Signal Processing)*, vol. 139, 147–159 (IET, 1992). Issue: 2.

4. Hanssen, R. F. *Radar Interferometry: Data Interpretation and Error Analysis*, vol. 2 (Springer Science & Business Media, 2001).

5. Menke, W. *Geophysical Data Analysis: Discrete Inverse Theory* (Academic press, 2018), fourth edn.

6. Fukushima, Y. & Hooper, A. Crustal deformation after 2004 Niigataken-Chuetsu earthquake, central Japan, investigated by persistent scatterer interferometry. *J. Geod. Soc. Jpn.* **57**, 195–214 (2011). In Japanese with English abstract.

7. Takada, Y., Sagiya, T. & Nishimura, T. Interseismic crustal deformation in and around the Atotsugawa fault system, central Japan, detected by InSAR and GNSS. *Earth, Planets Space* **70**, DOI: 10.1186/s40623-018-0801-0 (2018).

8. Chilès, J.-P. & Delfiner, P. *Geostatistics: Modeling Spatial Uncertainty*. Wiley series in probability and mathematical statistics; Applied probability and statistics (Wiley, 1999).

9. Oliver, M. A. & Webster, R. *Basic Steps in Geostatistics: The Variogram and Kriging*. SpringerBriefs in Agriculture (Springer Cham, 2015).

10. Ou, Q. *et al.* Large-scale interseismic strain mapping of the NE Tibetan Plateau from Sentinel-1 interferometry. *J. Geophys. Res. Solid Earth* **127**, DOI: 10.1029/2022JB024176 (2022).

11. Sudhaus, H. & Jónsson, S. Improved source modelling through combined use of InSAR and GPS under consideration of correlated data errors: Application to the June 2000 Kleifarvatn earthquake, Iceland. *Geophys. J. Int.* **176**, 389–404, DOI: 10.1111/j.1365-246X.2008.03989.x (2009). Publisher: Oxford University Press.

12. Hamzehpour, N. & Bogaert, P. Improved spatiotemporal monitoring of soil salinity using filtered kriging with measurement errors: An application to the West Urmia Lake, Iran. *Geoderma* **295**, 22–33, DOI: 10.1016/j.geoderma.2017.02.004 (2017). Publisher: Elsevier B.V.

13. Kobayashi, T., Morishita, Y. & Yarai, H. SAR-revealed slip partitioning on a bending fault plane for the 2014 Northern Nagano earthquake at the northern Itoigawa–Shizuoka tectonic line. *Tectonophysics* **733**, 85–99, DOI: 10.1016/j.tecto.2017.12.001 (2018).

14. Shen, Z.-K., Jackson, D. D. & Ge, B. X. Crustal deformation across and beyond the Los Angeles. basin from geodetic measurements. *JOURNAL OF GEOPHYSICAL RESEARCH* **101**, 957–984 (1996).

15. Sagiya, T., Miyazaki, I. & Tada, T. Continuous GPS array and present-day crustal deformation of Japan. *Pure Appl. Geophys.* **157**, DOI: 10.1007/PL00022507 (2000).

Orbit	Path	Frame	Beam ID (off nadir angle in degree)
Ascending	126	710, 720	RU2_6 (29.1)
Ascending	126	710, 720	RU2_7 (32.4)
Ascending	126	710, 720, 730	RU2_8 (35.4)
Ascending	126	720, 730	RU2_9 (38.2)
Descending	19	2870, 2880	RU2_7 (32.4)
Descending	19	2870, 2880, 2890	RU2_8 (35.4)
Descending	19	2880, 2890	RU2_9 (38.2)
Descending	20	2880, 2890	RU2_7 (32.4)

Table S1. Details of the SAR data.

Name	Period	# of stations	Software	Strategy	Ocean load model	Reference frame
GEONET	2021-01-01 2023-12-31	119	Gipsy-X Ver. 1.4	PPP+AR	FES2014b	ITRF 2014
University	2021-01-01 2023-12-31	13	Gipsy-X Ver. 1.4	PPP+AR	FES2014b	ITRF 2014
SB	2021-05-02 2023-12-31	315	Gipsy-X Ver. 2.2	PPP+AR	NAO99b	ITRF 2014

Table S2. Details of the GNSS data processing.
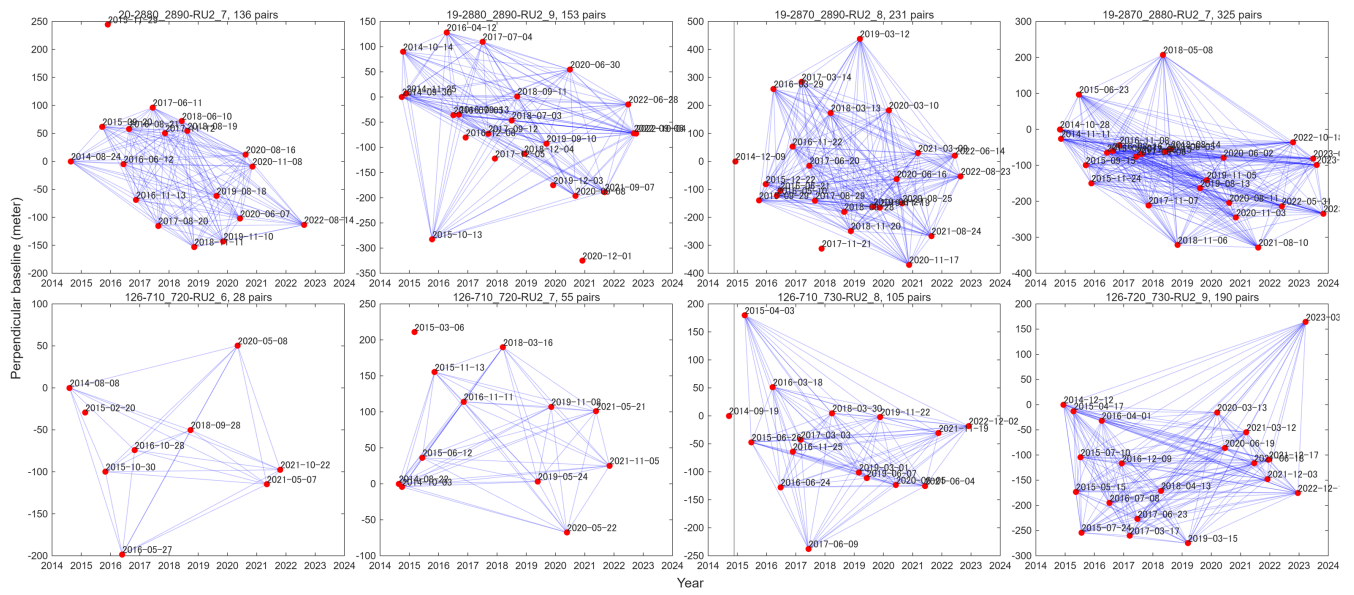
Figure S1. Time-perpendicular baseline diagram for the InSAR dataset. The red dots indicate data acquisition dates. The blue lines denote the interferograms used in this study. The vertical lines indicate the date of the 2014 northern Nagano earthquake (Figure 1c).
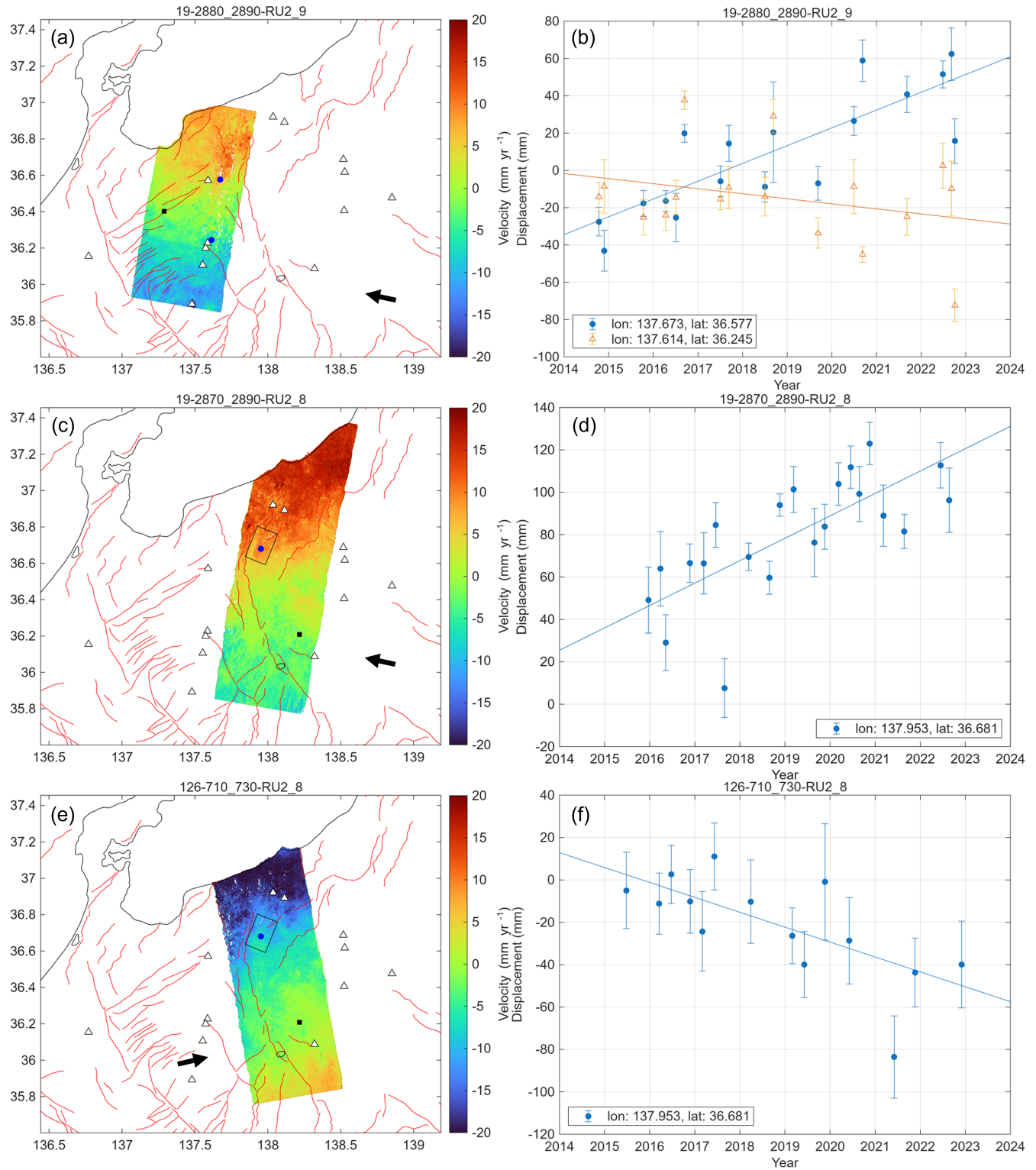
Figure S2. Example of InSAR line-of-sight (LOS) time series. (**a,c,e**) Average velocities toward the satellite. The black dot indicates the reference point and the black arrow shows the satellite LOS direction. The white triangles indicate Holocene volcanoes and the red lines represent active fault traces. The black rectangle in (**c,e**) shows the location of the fault model of the 2014 northern Nagano earthquake[13]. (**b,d,f**) LOS time series at the blue dots shown in (**a,c,e**). The error bars represent standard deviations (Supplementary Text S1). The slope of the fitted line corresponds to the average velocities plotted in (**a,c,e**). Details of the data are provided in Supplementary Table S1.
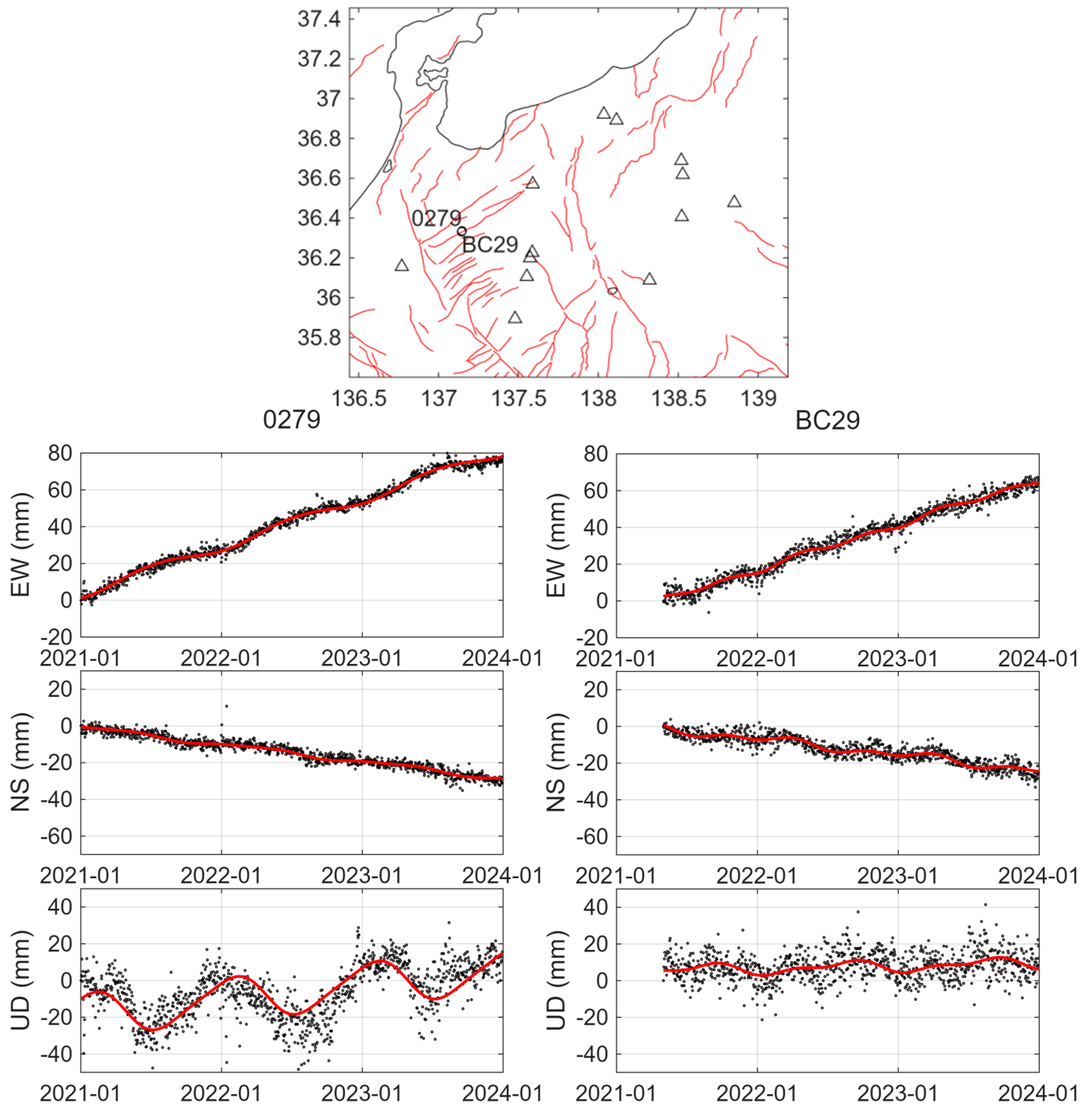
Figure S3. Example of GNSS time series. Top panel shows the location of the stations: 0279 (GEONET) and BC29 (SB). Distance between the stations is < 600 m. Bottom panels show the time series of 0279 and BC29. The red lines indicate the regression results (Equation 1).
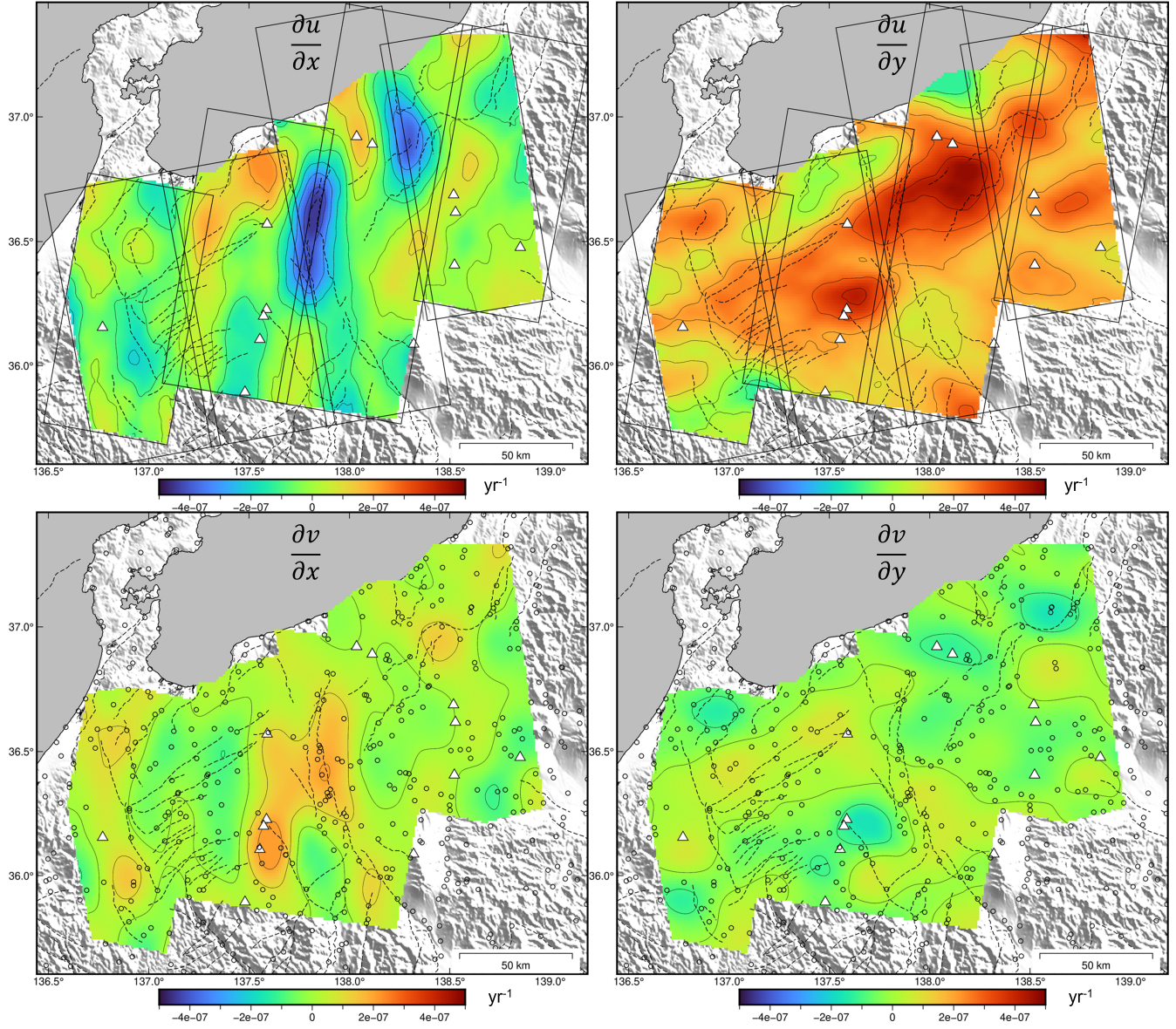
Figure S4. Estimated velocity gradients from eastward (InSAR) and northward (GNSS) velocities (u, v). The east-west and north-south coordinates are indicated as x, y, respectively. The radius R is set to 15 km.
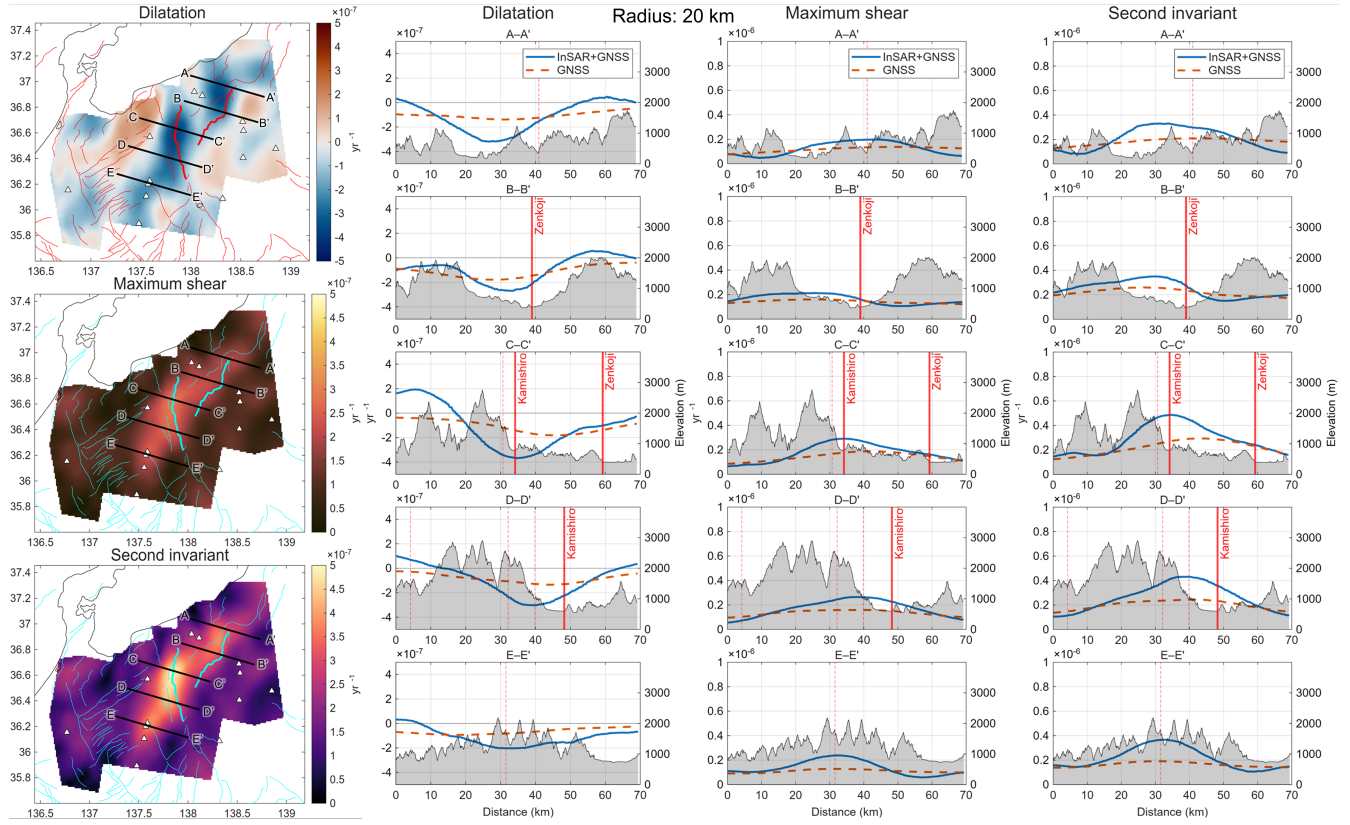
Figure S5. Strain rates along the profiles ($R = 20$ km). Descriptions are the same as Figure 6.
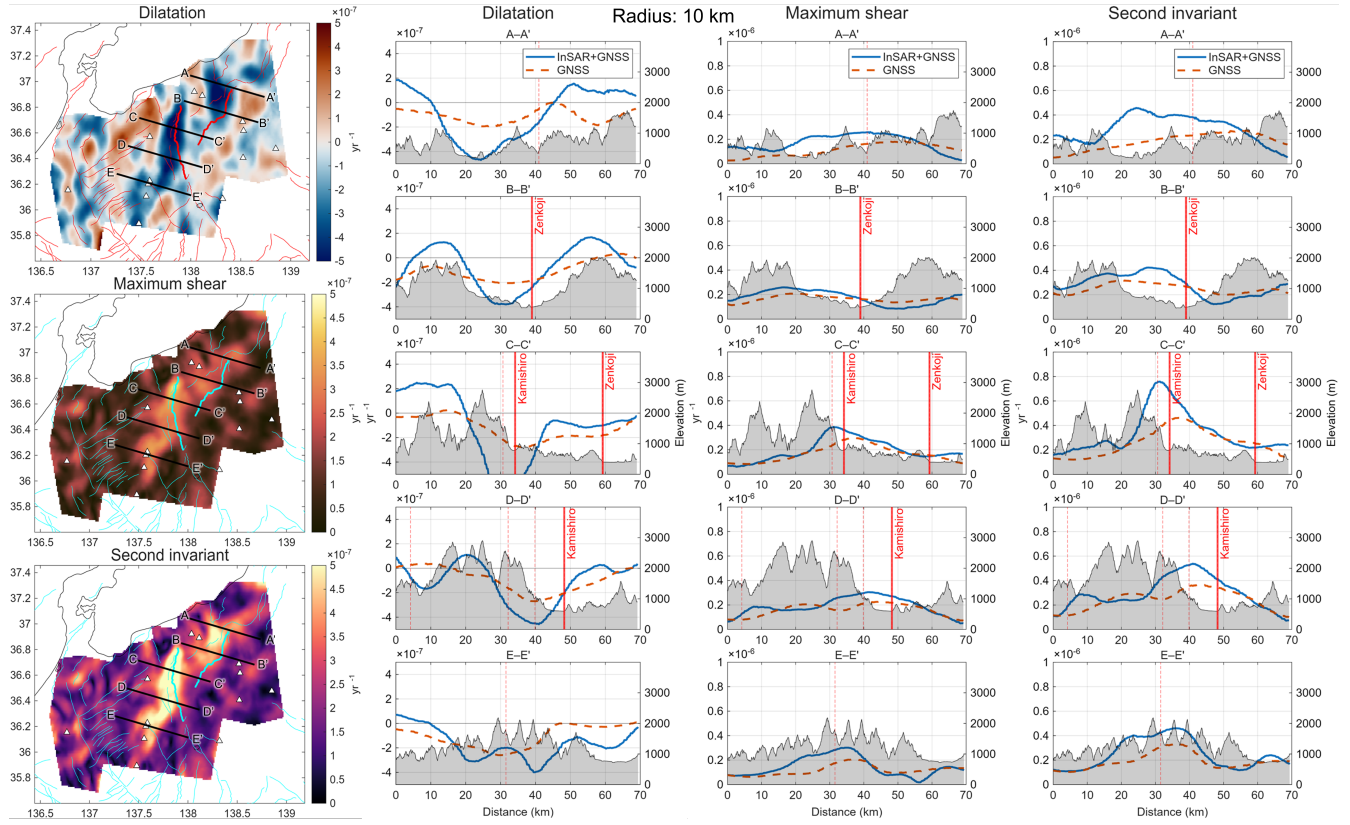
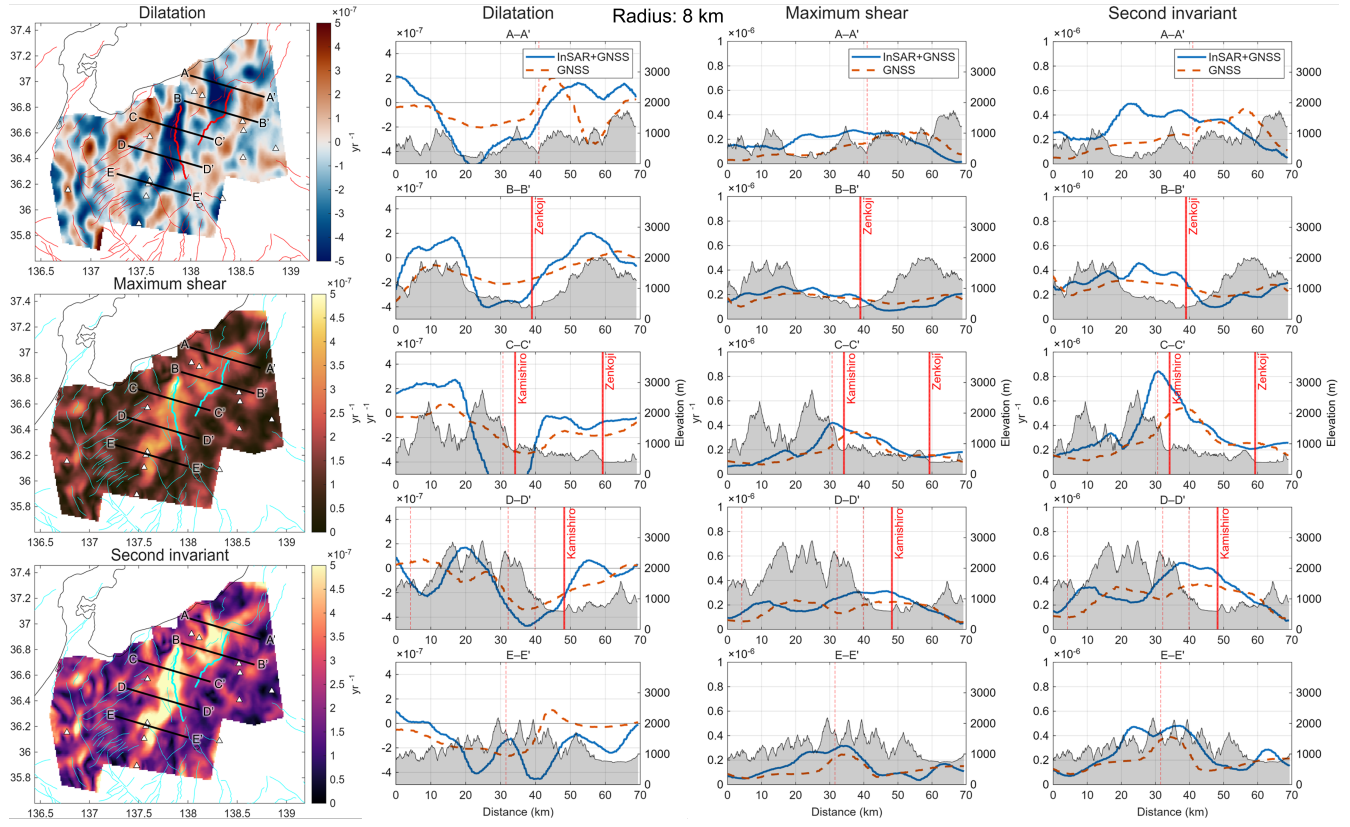**Figure S6.** Strain rates along the profiles ($R = 10$ km). Descriptions are the same as Figure 6.

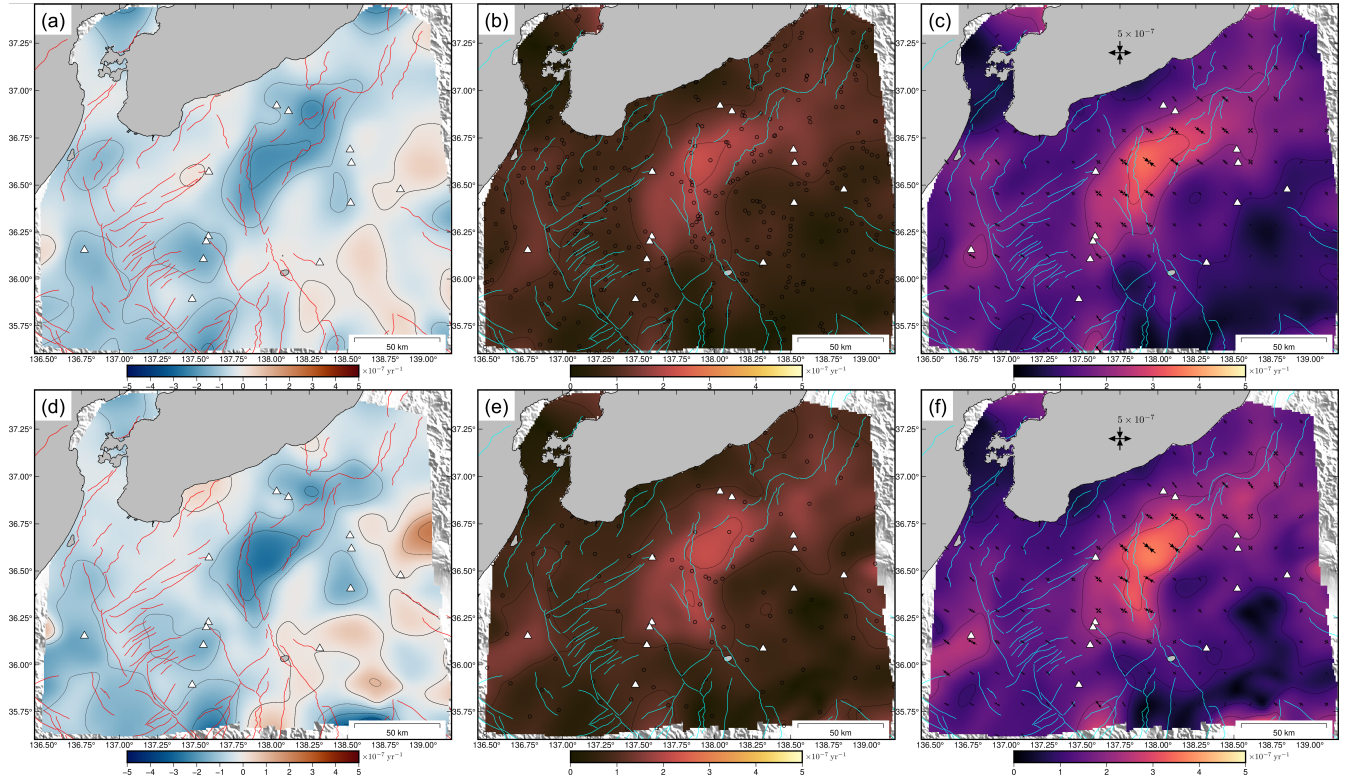**Figure S7.** Strain rates along the profiles ($R = 8$ km). Descriptions are the same as Figure 6.

Figure S8. GNSS strain rates estimated by a conventional method[14, 15]. The distance decay constant is set to 15 km. (**a**–**c**) Invariants of the strain tensor (dilatation, maximum shear, and second invariant), calculated from the all GNSS networks (GEONET, University, SB). (**d**–**f**) Invariants of the strain rate tensor, calculated from the GEONET stations only. The black open circles in (**b**) and (**e**) show the location of the GNSS stations. The coupled black arrows in (**c**) and (**f**) denote magnitude and directions of the principal strain rates. The white triangles indicate Holocene volcanoes. Red and cyan lines indicate active fault traces. The contour interval is $1 \times 10^{-7} \, \mathrm{yr}^{-1}$.
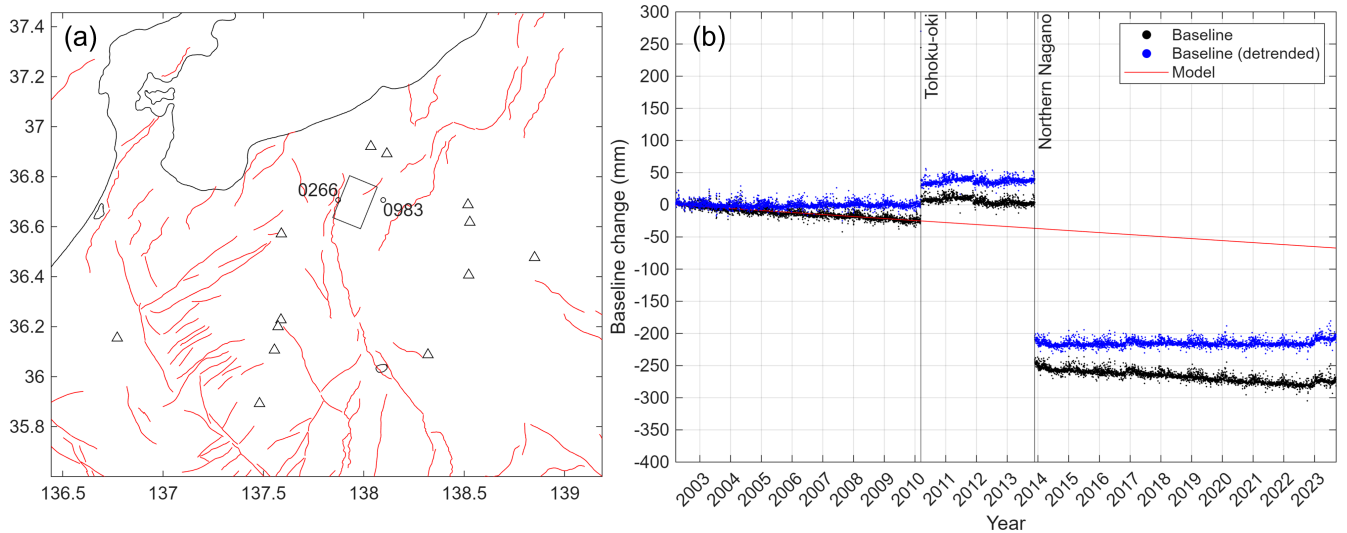

Figure S9. GNSS baseline length change. (**a**) Station locations. Inter-station distance is ~ 20 km. The black rectangle shows the location of the fault model of the 2014 northern Nagano earthquake[13]. The white triangles mark Holocene volcanoes and the red lines indicate active fault traces. (**b**) Baseline length change. The black dots represent the baseline length time series. The red line denotes a linear trend estimated from the data before the 2011 Tohoku-Oki earthquake and the blue dots indicate detrended time series.
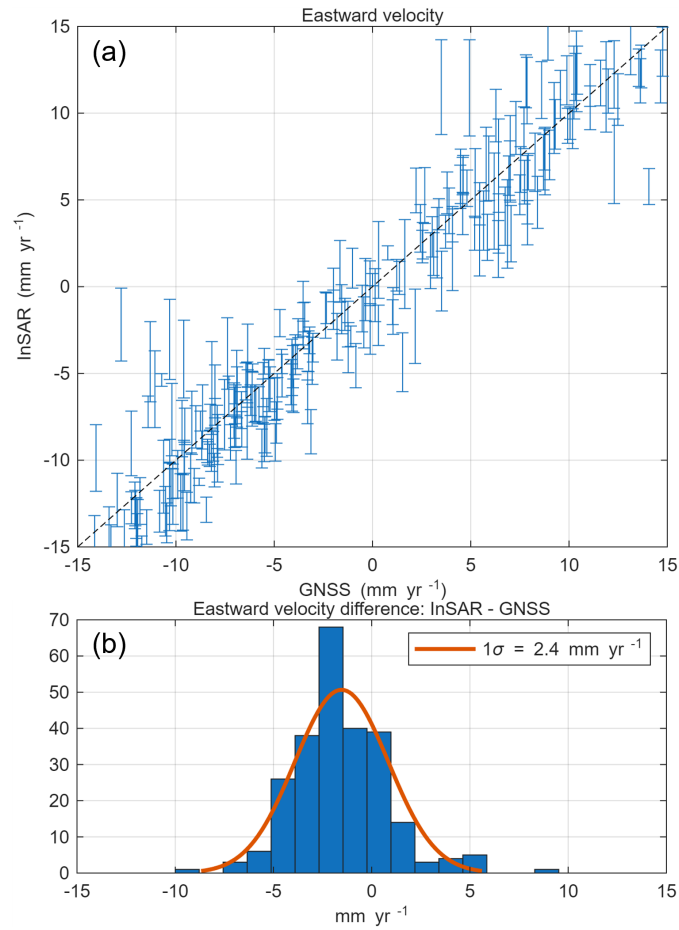
Figure S10. Comparison between InSAR- and GNSS-derived eastward velocities. (**a**) Scatter plot of InSAR versus GNSS velocities. The black dashed line indicates the 1:1 correspondence between the two measurements. (**b**) Histogram of the velocity differences between InSAR and GNSS. The orange curve represents the best-fitting normal distribution.
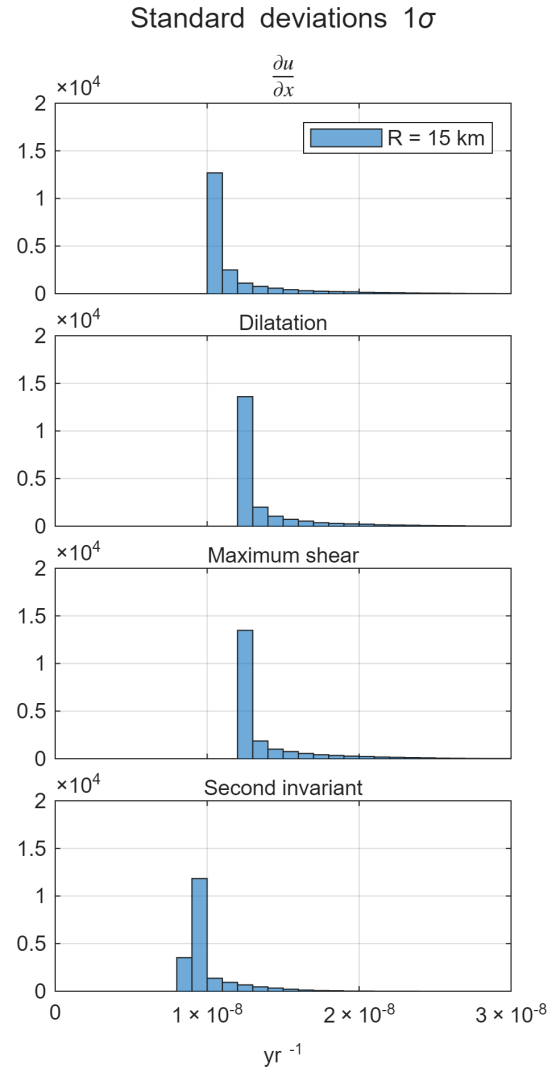
Figure S11. Histogram of the estimated standard deviations for the strain rate fields. The radius *R* is set to 15 km (Supplementary Texts S1, S3, and S4).
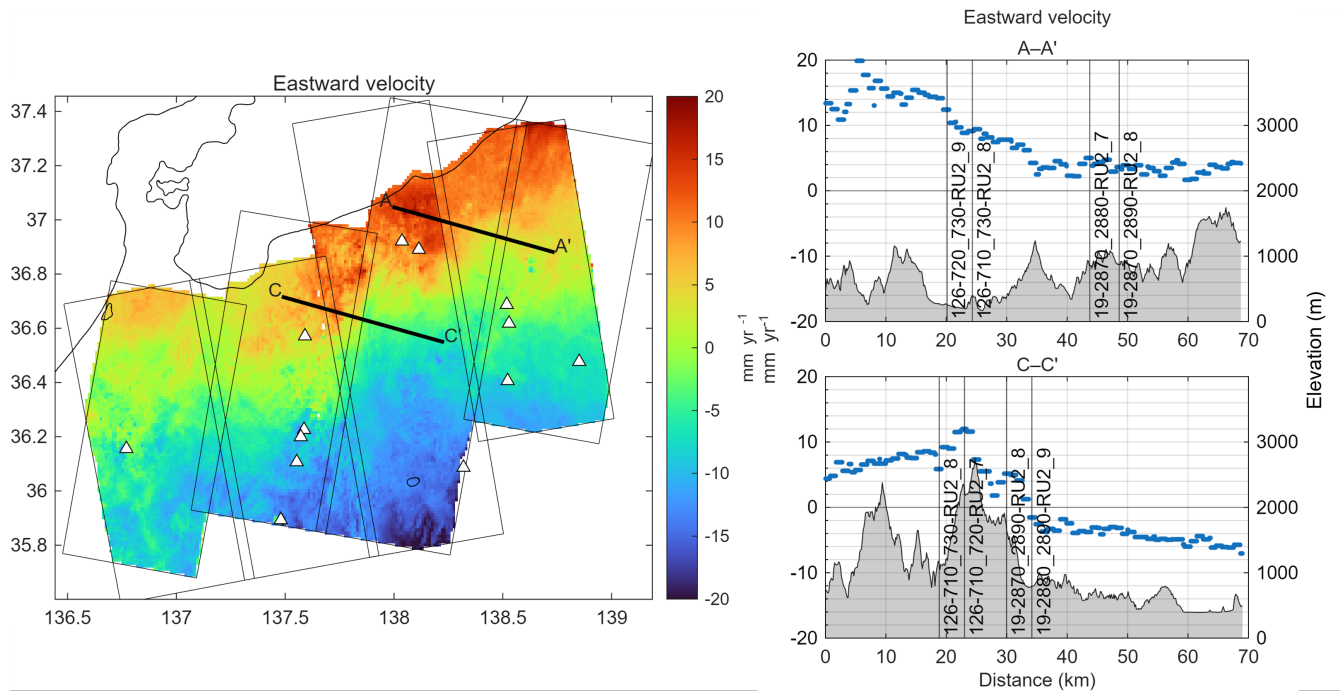
Figure S12. Left: InSAR eastward velocity. The black rectangle shows SAR acquisition frames. Right: InSAR eastward velocity along the profiles. The vertical lines indicate the edges of SAR frames. The black line with shaded area shows elevation in meters.
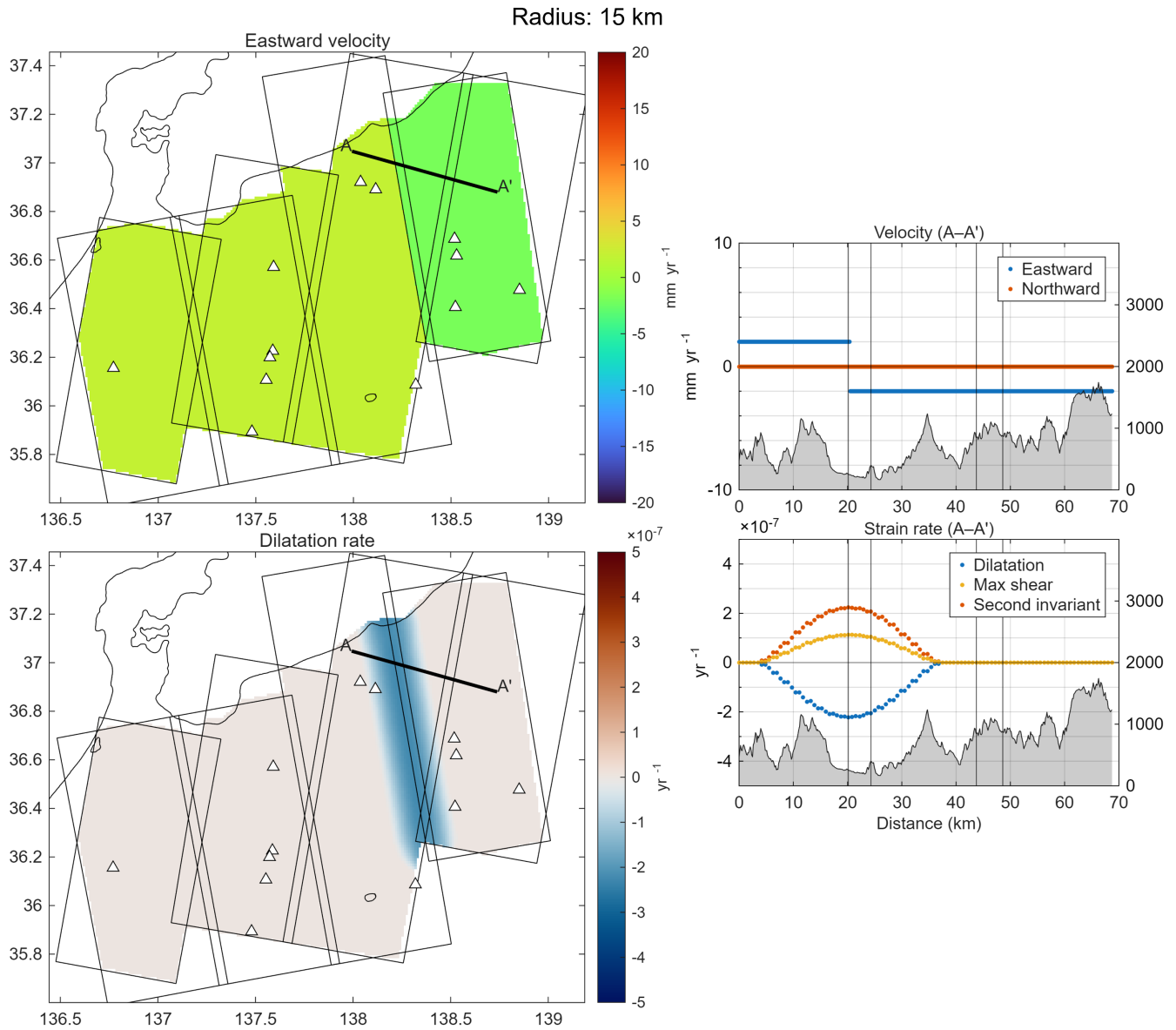
Figure S13. Effect of a swath gap in the strain rate estimates. Top left: an artificial velocity map (eastward), with a gap of 4 mm yr^{-1}. The black rectangles show SAR acquisition frames. Bottom left: corresponding strain rate (dilatation rate), calculated in the same method ($R = 15$ km). Top right: eastward and northward velocities along the profile. Bottom right: profile of the corresponding strain rates. The vertical lines indicate the location of the SAR frame edges. The black line with shaded area shows elevation.